*Carbon Energy*

WILEY

CARBON ENERGY

RESEARCH ARTICLE OPEN ACCESS

# Ultrahigh-Mass-Loading Electrodes With Enhanced Homogeneity Using a High-Concentration Slurry for Lithium-Ion Batteries

Jun Kyu Park[1,2] | Woohyeon Shin[1] | Woohyeon Jo[3] | Hyo-Jeong Lee[4] | Won-Yong Jeon[5] | Jinho Ahn[6] | Jihee Yoon[7] | Yea-Ji Jeong[5] | Joonyoung Oh[8] | Minji Kang[8] | Min-Jae Choi[5] | Jin Joo[2] | Jongsoon Kim[6] | Seong-Keun Cho[8] | Jun Dong Park[4] | Jaewook Nam[3,9] | Jung-Keun Yoo[1]

[1]Energy Storage Research Center, Korea Institute of Science and Technology (KIST), Seoul, Republic of Korea | [2]Department of Applied Chemistry, Kyungpook National University, Daegu, Republic of Korea | [3]Department of Chemical and Biological Engineering, Seoul National University, Seoul, Republic of Korea | [4]Department of Chemical and Biological Engineering, Sookmyung Women's University, Seoul, Republic of Korea | [5]Department of Chemical and Biochemical Engineering, Dongguk University, Seoul, Republic of Korea | [6]Department of Energy Science, Sungkyunkwan University, Suwon, Gyeonggi-do, Republic of Korea | [7]Composites Research Division, Carbon Composites Department, Korea Institute of Materials Science (KIMS), Changwon, Gyeongsangnam-do, Republic of Korea | [8]Chemical Materials Solutions Center, Korea Research Institute of Chemical Technology (KRICT), Daejeon, Republic of Korea | [9]Institute of Chemical Processes, Seoul National University, Seoul, Republic of Korea

**Correspondence:** Jun Dong Park (jdpark@sookmyeong.ac.kr) | Jaewook Nam (jaewooknam@snu.ac.kr) | Jung-Keun Yoo (yoojk@kist.re.kr)

**Received:** 25 March 2025 | **Revised:** 12 August 2025 | **Accepted:** 16 August 2025

**Keywords:** cathodes | dispersibility | dispersion solution | high-mass-loading | lithium-ion batteries

## ABSTRACT

Strategies for achieving high-energy-density lithium-ion batteries include using high-capacity materials such as high-nickel NCM, increasing the active material content in the electrode by utilizing high-conductivity carbon nanotubes (CNT) conductive materials, and electrode thickening. However, these methods are still limited due to the limitation in the capacity of high-nickel NCM, aggregation of CNT conductive materials, and nonuniform material distribution of thick-film electrodes, which ultimately damage the mechanical and electrical integrity of the electrode, leading to a decrease in electrochemical performance. Here, we present an integrated binder-CNT composite dispersion solution to realize a high-solids-content (> 77 wt%) slurry for high-mass-loading electrodes and to mitigate the migration of binder and conductive additives. Indeed, the approach reduces solvent usage by approximately 30% and ensures uniform conductive additive-binder domain distribution during electrode manufacturing, resulting in improved coating quality and adhesive strength for high-mass-loading electrodes (> 12 mAh $cm^{-2}$). In terms of various electrode properties, the presented electrode showed low resistance and excellent electrochemical properties despite the low CNT contents of 0.6 wt% compared to the pristine-applied electrode with 0.85 wt% CNT contents. Moreover, our strategy enables faster drying, which increases the coating speed, thereby offering potential energy savings and supporting carbon neutrality in wet-based electrode manufacturing processes.

## 1 | Introduction

The approaches for improving the energy density of NCM-type lithium-ion batteries (LIBs) are largely classified into applying high-energy-density active materials [1–3], increasing the ratio of active materials in the electrode [4–9], and electrode thickening [10–13]. Applying high-energy-density active materials can improve the capacity by increasing the nickel content in

Jun Kyu Park, Woohyeon Shin and Woohyeon Jo equally contributed to this study

NCM-type LIBs. In the case of ternary cathode materials, which are mainly used as cathode materials for electric vehicles, the increase in nickel content acts as a major factor that reduces the lifespan and stability of the LIBs [3]. In addition, as the nickel content has currently reached over 90%, practical application involves challenging issues, including anisotropic lattice volume change derived from abrupt shrinkage with H2–H3 transformation [14] and excessive growth of the cathode-electrolyte interface ascribed to severe side reactions at the electrode-electrolyte interface [15].

Due to limitations of high-capacity Ni-rich NCM-type active materials, such as electrochemical performance degradations ascribed to structural collapse and severe side reactions with electrolytes, electrode structure engineering, including maximizing the active material ratio [4–9] and electrode thickening [10–13], must continue to be explored for the development of high-performance NCM-type LIBs [16, 17]. Particularly, electrode structure engineering for NCM-type LIBs needs to be carried out more in depth and systematically than currently practiced, and requires original process design [18]. Furthermore, because of the global battery overheating competition, including in the Tesla, LG energy solution, SKon, Samsung SDI, CATL, and BYD, electrode structure engineering focusing on economic efficiency values such as process advantages and cost is an essential consideration in future battery electrode design [19, 20].

From the perspective of electrode structure design, increasing the active material ratio within the electrode [4–9] and thickening the electrode [10–13] layer are essential for enhancing the energy density of the battery. The increase in the ratio of active material in the electrode is realized by decreasing the ratio of inactive materials, such as conductive materials and binders. Especially, ideal electrode thickening reduces the stack by thickening the cathode loading itself, thereby lowering the total ratio of the separator and current collector within the thick film electrode. The conventional thin electrode design increases the cathode loading within the electrode by stacking multiple stacks. However, the total ratio of the separator and current collector within the electrode also increases as the number of stacks increases, limiting energy density improvement [16].

Even though the studies described above have contributed toward increasing the thickness of electrodes for manufacturing high-energy-density NCM-type LIBs, the binder migration during the drying process, which is the main wet process of LIBs manufacturing, is still an issue that needs to be resolved. The binder migration is a phenomenon in which the binder floats to the electrode surface by capillary action as the 1-methyl-2-pyrrolidinone (NMP) solvent evaporates during the drying process, and the carbon-binder domain (CBD) distribution within the electrode becomes uneven, which is the main cause of the decrease in the electrode's integrity and electrolyte impregnation [21]. In addition, the binder migration phenomenon becomes particularly severe in the electrode thickening process [22]. Therefore, to improve the uneven distribution of CBD within the electrode caused by binder unevenness, the NMP solvent content should be fundamentally reduced. However, reducing the NMP solvent content makes it difficult to disperse the conductive material and binder inside the electrode due to the increased slurry viscosity. The reduction in the NMP solvent content results in the problem of uneven distribution of CBD inside the electrode before the drying process.

In this contribution, we present a high-concentration slurry based on an integrated binder-CNT dispersion (IBC) solution as an approach to realize uniform CBD distribution and facile electrode thickening for high-energy-density LIBs (Figure 1). The electrode fabrication process consists of mixing, coating, drying, and calendaring processes, and a slurry with active materials, conductive agents, and binders is fabricated in the mixing process. Conventional slurries individually mix active materials, conductive agent dispersions, and binder dispersions. In this study, we fabricated electrodes using an IBC solution in which conductive agents and binders are well dispersed, and we systematically investigated the electrode-related physical properties, including CBD distribution and electrochemical performances by comparing them with electrodes fabricated with individual dispersion solution (pristine). In rheological characterization, the slurry applied by the IBC solution showed high viscosity, dramatic shear thinning behavior, and high dispersibility. In the mixing process, the presented slurry could reduce the total NMP content while increasing the maximum solid content to 77 wt% compared to 70 wt% of the slurry manufactured with the pristine. It was ultimately possible to manufacture a high-concentration slurry and realize high-mass–loading electrodes ( $> 12\ \mathrm{mAh\ cm^{-2}}$). The prepared electrode showed a uniform CBD distribution, excellent adhesive properties, and low electrical resistance. In addition, the presented electrode showed outstanding cyclability with a capacity retention of 77.6% after long-term cycling, whereas the pristine-applied electrode achieved a capacity retention of only 68.4% under the same conditions. Beyond the same composition, the electrode in which the IBC solution was applied showed excellent electrochemical performance despite the low carbon nanotube (CNT) contents of 0.6 wt% compared to the electrode in which the conventional individual dispersion with 0.85 wt% CNT contents was applied. Therefore, to realize the ideal thick electrode design, a prerequisite is to fabricate a high-concentration slurry by increasing the total solid content in the slurry. From an industrial perspective, the realization of a high-concentration slurry can reduce the NMP solvent content in the mixing process, improve the coating quality by minimizing the side-edge effect in the coating process, and lower the binder migration ascribed to the capillary phenomenon of the NMP solvent in the drying process. Furthermore, the above series of advantages in the respective processes of a high-concentration slurry can eventually lead to the production of high-quality electrodes and reduction in energy loss. Beyond the industrial perspective, the approach involving a high-concentration slurry is economically efficient and environmentally friendly due to the reduction of installation costs, processing costs, processing time, and energy in the drying and recovery process ascribed to the reduction of NMP solvent contents.

## 2 | Results and Discussion

In the wet process of LIBs, the rheological properties of the slurry are important factors that determine the coating quality [23, 24]. In particular, the viscosity of the slurry at the stationary

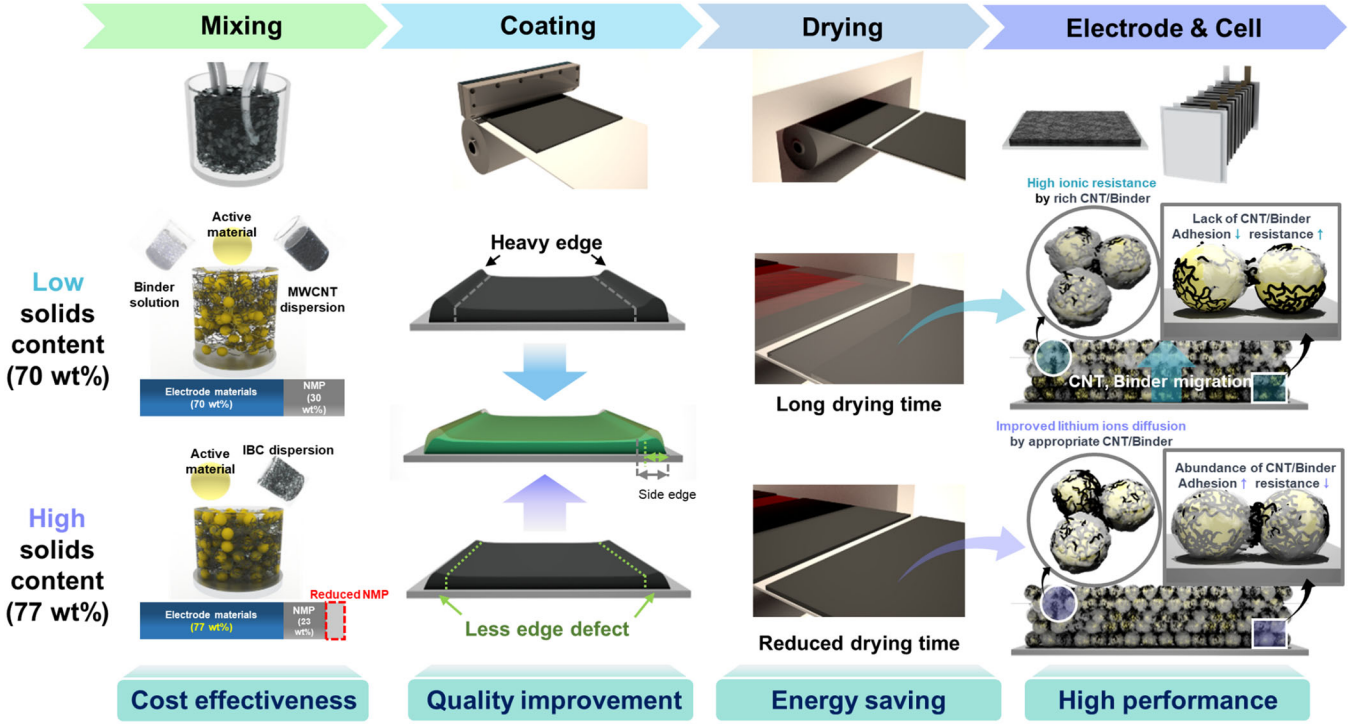


**FIGURE 1** | Schematic illustration of comparison by electrodes' manufacturing process; pristine-applied electrode with low-solids content (70 wt%) and IBC solution-applied electrode with high-solids content (77 wt%).

phase and the viscosity corresponding to the shear rate of 10–100 $s^{-1}$ are directly related to the coating speed, edge thickness, and CBD distribution of the slurry [20, 25]. For coating and drying process advantages, including high coating speed, small edge thickness, and uniform CBD distribution, we introduced an IBC solution into the slurry (Figure S1). In the rheological characterization, the IBC solution showed higher viscosity at the stationary phase and lower viscosity at the shear rate of 10–100 $s^{-1}$ compared to pristine and showed more dramatic shear-thinning behavior (Figure 2A) as well as more solid-like behavior based on the lower phase shift angle value (Figure 2B). In addition, yield stress and zeta potential are widely utilized as representative indicators of the dispersibility of the suspension [26, 27]. The yield stress (τ0) of the IBC solution was calculated from the viscosity (η), shear stress (τ), and shear rate ($\dot{\gamma}$) flow curve data based on the Casson model (Equation 1) and was lower than that of the pristine solution (Figure 2C) [28, 29]. Moreover, the IBC solution also has a higher zeta potential (~ 46.1 mV) compared to the pristine-applied solution (~ 32.1 mV) (Figure S2). Therefore, the yield stress and zeta potential demonstrate a more stable dispersion state in the IBC solution. The pristine-applied slurry has a maximum solid content of 70 wt%, and when it increases above 70 wt%, the coating process is difficult due to the high viscosity in the shear rate range of 10–100 $s^{-1}$. On the other hand, the IBC solution-applied slurry had a low viscosity in the shear rate range of 10 to 100 $s^{-1}$ even at a maximum solid content of 77 wt %, so the coating process could be applied. Compared with the pristine-applied slurry, the IBC solution-applied slurry showed dramatic shear-thinning behavior, low phase shift angle, and low yield stress despite the 7 wt% higher solid content, showing potential for high-speed coatings such as slot die coating and comma coating (Figure 2D–F) [30].

$$\sqrt{\tau} = \sqrt{\tau 0} + \sqrt{\eta \dot{\gamma}} \quad (1)$$

The IBC solution-applied slurry shows a distinctive rheological profile with more pronounced shear-thinning behavior compared to the pristine-applied slurry. This profile has higher viscosity at low shear rates and lower viscosity at high shear rates, indicating superior stability and processability: the slurry flows easily inside the small coating gap (typically 100 μm). As the coated slurry exits the coating dies and the applied shear rapidly diminishes, the slurry viscosity increases significantly, effectively fixing the shape of the coated layer. This rapid increase in viscosity preserves the electrode layer morphology, suppressing capillary-driven flows that typically cause surface defects such as ridge formation, known as the heavy-edge effect [31]. The higher viscosity at low shear rates prevents sedimentation and aggregation of solid constituents during storage while supporting uniform, durable coating layer formation after application [32–35]. This increased viscosity also inhibits undesirable particle or binder migration during drying [34, 35]. Simultaneously, reduced viscosity at high shear rates facilitates efficient mixing and coating operations, enhancing overall slurry processability [32–35].

Indeed, the heavy-edge effect of the proposed IBC solution-applied slurry in the blade coating system (Figure 2G) was systematically investigated based on four quality parameters in presented previous studies [36], including dimensionless width ($B^*$), dimensionless gap ($G^*$), dimensionless height ($H^*$), and edge slope ($R^*$) (Figure 2H,I). The bulk height is denoted as $H_{coat}$, which is lower than the height near the edge ($H_{edge}$) because of the presence of a heavy edge. The width of the edge can be expressed in two different ways. $W_{side}$ represents the

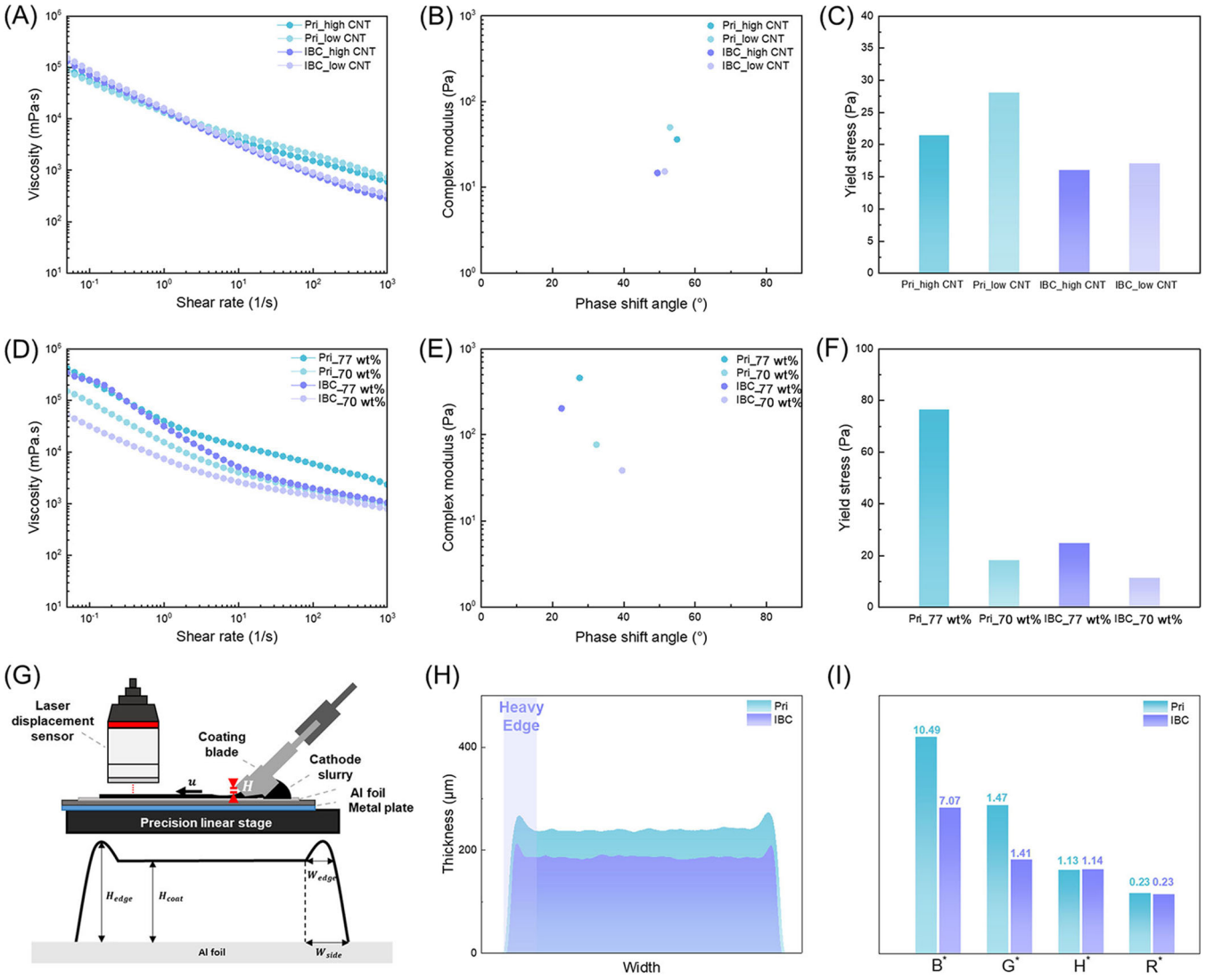


**FIGURE 2** | Correlation between rheological properties and coating quality. (A) Flow curve and (B) phase shift angle of a pristine binder-conductive additive mixing solution and IBC solution. The phase shift angle was calculated at an angular frequency $\omega = 6.3\ \text{rad s}^{-1}$. (C) Yield stress using the Casson model. (D) Flow curve, (E) phase angle, and (F) yield stress of a pristine-applied slurry and an IBC solution-applied slurry. (G) Schematic illustration of the blade coating system. (H) Wet profile of the coated cathode slurry with different coating gaps ($H$): 350 μm for the pristine-applied slurry and 260 μm for the IBC solution-applied slurry. (I) Coating quality parameters. The coating process was performed at a speed of $3\ \text{m min}^{-1}$ and a blade width of 25 mm.

width from the edge profile to the bulk height, whereas $W_{\text{edge}}$ is the width in the region where the height of the edge exceeds the bulk height (Figure 2G).

To analyze the heavy-edge effect, the dimensionless height can be expressed as follows:

$$H^* = \frac{H_{\text{edge}}}{H_{\text{coat}}} \tag{2}$$

$H^*$ is the ratio of the relative height of the heavy edge to the coated height. In addition, the dimensionless width $B^*$, which is the relative width of the heavy edge to the coated height, was defined and used as follows:

$$B^* = \frac{W_{\text{edge}}}{H_{\text{coat}}} \tag{3}$$

The slope of the heavy edge, $R^*$, was also calculated based on previous studies.

$$R^* = \frac{H_{\text{coat}}}{W_{\text{side}} - W_{\text{edge}}} \tag{4}$$

Finally, in order to obtain the correlation between the coating gap, $H$, and the bulk height of the slurry, $H_{\text{coat}}$, the dimensionless gap, $G^*$, was defined for the analysis of the results.

$$G^* = \frac{H}{H_{coat}} \quad (5)$$

The quality parameters were obtained by averaging those from the left and right edges. There were no remarkable differences in the dimensionless height ($H^*$) and edge slope ($R^*$) for both cathode slurries. However, the dimensionless width ($B^*$) decreases in the IBC solution-applied slurry. During the coating process, there is a significant shear rate change through the coating gap, which rapidly decreases after the coating process. In other words, when the coated slurry shape is determined, the viscosity of the slurry increases to stationary-phase viscosity. As shown in the above results, the high viscosity (at a shear rate of 0.1 $s^{-1}$) and the low phase-shift angle of the IBC solution-applied slurry maintain the structure of the slurry and reduce the heavy-edge effect in the coating process. In addition, the dimensionless gap ($G^*$) decreases in the IBC solution-applied slurry, which implies that the coating thickness would be thicker when coating with the same coating gap. Even at the same gap of 350 μm, the same trend appears and it is confirmed that the heavy-edge effect can be suppressed with the IBC solution-applied slurry (Figure S3).

The increase in the maximum solid content to 77 wt% by introducing the IBC solution suggests the possibility of shortening the drying time in the drying process [37]. Indeed, when investigating the time required for the NMP solvent to evaporate in the drying process, the pristine-applied electrode required 86 s, whereas the IBC solution-applied electrode required 48 s, nearly reducing the drying time by half (Figure 3A) [38]. In addition, when looking at the drying state according to the coating speed of the comma coater, it was confirmed that the IBC solution-applied electrode reached the drying state faster than the pristine-applied electrode, even at a higher coating speed (Figure 3B). In the Electron Probe Micro Analyzer (EPMA) analysis to determine the CBD distribution of the electrode after the drying process, the pristine-applied electrode showed a lot of polyvinylidene fluoride (PVDF) in the upper layer of the electrode due to the excessive binder migration as the NMP solvent evaporated, whereas the IBC solution-applied electrode showed somewhat lower binder migration, showing a uniform CBD distribution (Figures 3C,D and S4). Notably, the IBC solution-applied electrode shows a uniform binder distribution with minimal binder migration, even under accelerated drying conditions. This behavior can be attributed to the higher viscosity of the IBC solution-applied slurry at low shear rates, which, as previously discussed, effectively suppresses binder migration during the drying process [34, 35].

Quantitatively, the pristine-applied electrode showed concentrated PVDF distribution in the middle and top layers, whereas the IBC solution-applied electrode showed a uniform PVDF distribution from the bottom to the top (Figure 3E) [39]. In addition, the morphology of the electrode was analyzed through 3D modeling based on the SEM images. The 3D modeling image showed that the pore volume of the pristine electrode was 26.41%, whereas that of the IBC electrode was 25.25%, showing similar pore volume ratios (Figure S5A,B). However, a significant difference was observed in the analysis based on 3D modeling (Figure S5C,D). Similar to EPMA results, a nonuniform solid distribution was observed in the pristine-applied electrode over the XY, YZ, and ZX axes, whereas a uniform solid distribution was observed in the IBC solution-applied electrode over the XY, YZ, and ZX axes. The above solid distribution results suggest that the binder and CNTs on the surface of the active material exist uniformly throughout the IBC solution-applied electrode thickness (uniform CBD distribution). The uniform CBD distribution of the IBC solution-applied electrode led to remarkable improvement in adhesion and cohesion compared to the pristine-applied electrode. The average adhesive peel strength of the IBC solution-applied electrode was approximately ~21.53 gf 20 $mm^{-1}$, which was approximately twice that of the pristine-applied electrode ( ~ 11.48 gf 20 $mm^{-1}$) (Figures 3F and S6A). The uniform CBD distribution was also evident in the cohesion test. The IBC solution-applied electrode showed more consistent cohesive peel strength than the pristine-applied electrode during multiple removals (Figures 3G and S6B). The IBC solution-applied electrode showed higher cohesion from the bottom to the top than the pristine state, but the opposite trend was observed on the electrode surface. Beyond the improved adhesion and cohesion, well-dispersed multi-walled carbon nanotubes (MWCNTs) due to a uniform CBD distribution within the electrode (Figure S7) increased the electrical conductivity and showed low resistivity, especially at an interfacial resistance of about ~0.91 Ω $cm^2$, which was about 48.4% that of the pristine-applied electrode ( ~ 1.88 Ω $cm^2$) (Figure S8).

The superior properties of a series of IBC solution–applied electrodes found at the electrode level were directly linked to electrochemical performances. At 2 C rate discharge capacity, the pristine-applied electrode showed a rate capacity of 66.62%, whereas the IBC solution-applied electrode showed an excellent rate capacity of 80.96% (Figures 4A and S9). Beyond the same CNT content, the pristine_high CNT applied electrode with additional CNT content (containing 0.85 wt% CNT content) showed a rate capacity of 79.00%, which was lower than that of the IBC solution-applied electrode (containing 0.6 wt% CNT content). The above results were supported in more depth based on the $Li^+$ ion diffusion coefficient and internal resistance during discharge. $Li^+$ ion diffusion is a measure directly related to the performance of LIBs, and the IBC solution-applied electrode showed higher $Li^+$ ion diffusion coefficients ($D_{Li+}$) than those of the pristine-applied electrode and pristine_high CNT-applied electrode over the entire voltage range (Figures 4B and S10) [40]. Here, $\tau$ denotes the current pulse duration time, while $m_B$ and $M_B$ represent the mass and molar mass of the host material, respectively. In addition, $V_M$ is the molar volume of the host material, and $S$ refers to the geometric area of the electrode. The terms $\Delta E_s$ and $\Delta E_t$ correspond to the voltage changes induced by the pulse and by the constant current charge-discharge processes, respectively.

$$D = \frac{4}{\pi\Delta\tau}\left(\frac{m_B V_M}{M_B S}\right)^2\left(\frac{\Delta E_S}{\Delta E_\tau}\right)^2 \quad (6)$$

Furthermore, the cell containing the IBC solution-applied electrode showed lower internal resistances during discharge reactions (Figures 4C and S11). In terms of the $Li^+$ ion deposition, a significant amount of $Li^+$ ion did not penetrate the bottom of the electrode and was deposited on the top surface of the electrode. The reason for the top surface deposition phenomenon is that the rate-determining step in the lithiation/-delithiation process is a solid-state diffusion throughout the electroactive lattice [41]. When the $Li^+$ ion intercalates to the cathode from the electrolyte, the reaction rate slows down and

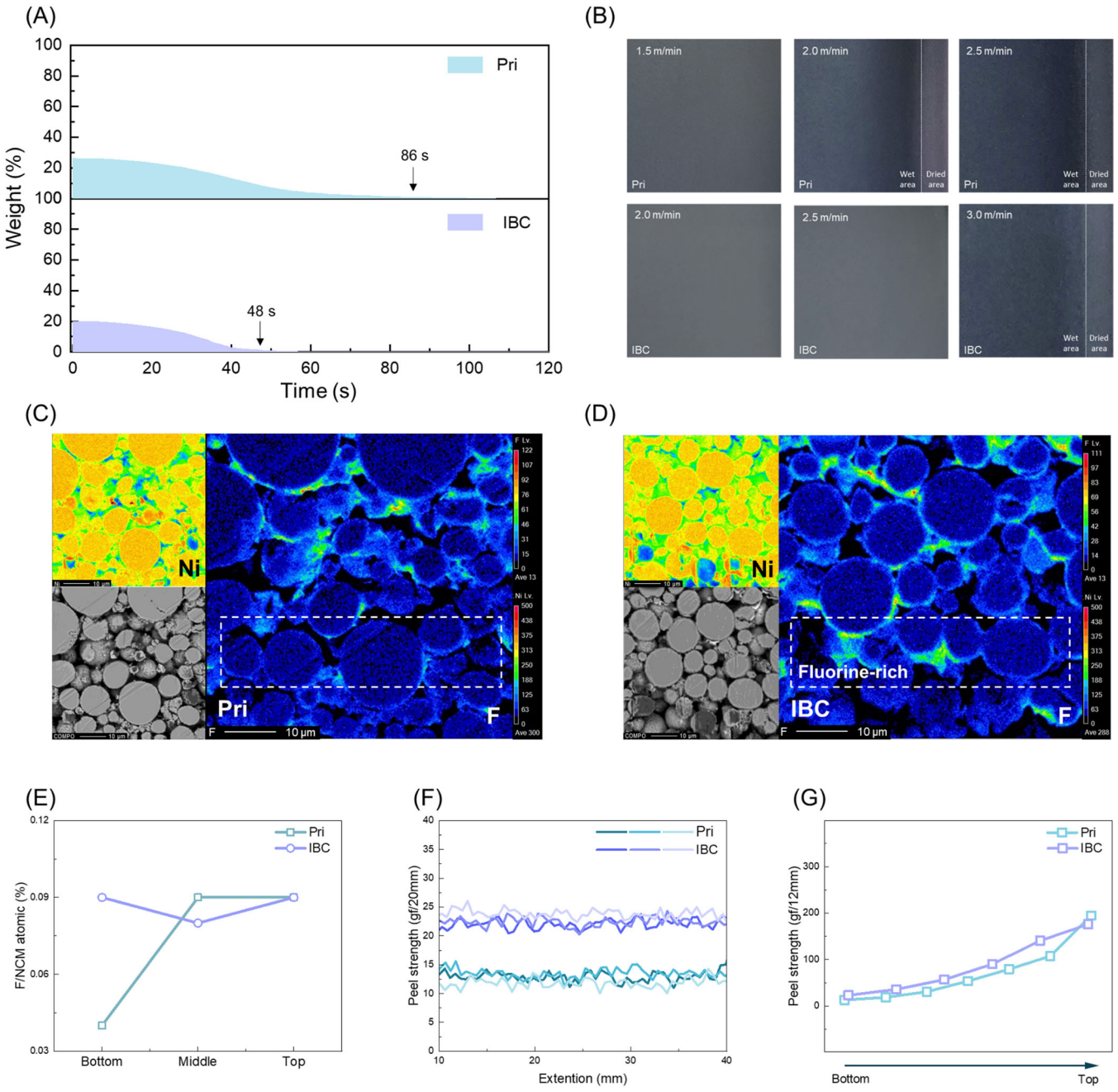


**FIGURE 3** | Observation of drying time in the electrode procedure and characterization of CBD distribution and mechanical strength in the electrode. (A) NMP contents during the drying process. (B) Electrode drying status with different coating speeds. The dashed line indicates the boundary between the dried and wet areas. (C), (D) EPMA analysis of elements' distribution of nickel and fluorine. (E) Comparison of the fluorine/-NCM atomic% of the electrodes. 90° peel tests of (F) adhesion and (G) cohesion strength.

they cannot move inside and inevitably react at the top surface of the electrode. At a press density of 2.8 g cc$^{-1}$ (Figure S12), $Li^+$ ion penetrated deep into the bottom of the electrode both the pristine-applied electrode and the IBC solution-applied electrode, which is the effect of the widened ion pathway due to the increased internal porosity of the electrode (Figure S13). When the porosity effect is minimized by increasing the press density to 3.2 g cc$^{-1}$, the pristine-applied electrode had $Li^+$ ion deficiency at the bottom because of CNT domain deficiency. On the other hand, IBC solution-applied electrodes with a uniform CBD distribution showed $Li^+$ ions even at the bottom and showed potential for reduction of $Li^+$ ion imbalance inside the electrode (Figure 4D,E). To further elucidate the difference of $Li^+$ penetration, confocal Raman analysis was performed. As the $E_g/A_{1g}$ intensity ratio of Raman spectra is affected by the degree of lithiation of the NCM, 4 points were observed along the electrode thickness direction (Figure S14). As a result of the measurement, the $E_g/A_{1g}$ ratio variation between the bottom and top was observed in the pristine-applied electrode, indicating a nonuniform $Li^+$ distribution along the electrode thickness (Figure S15) [42, 43]. It is implied that an IBC solution-applied electrode with a uniform CBD distribution is more suitable for the practical fabrication of a high-mass-loading electrode than a pristine-applied electrode. Indeed, in

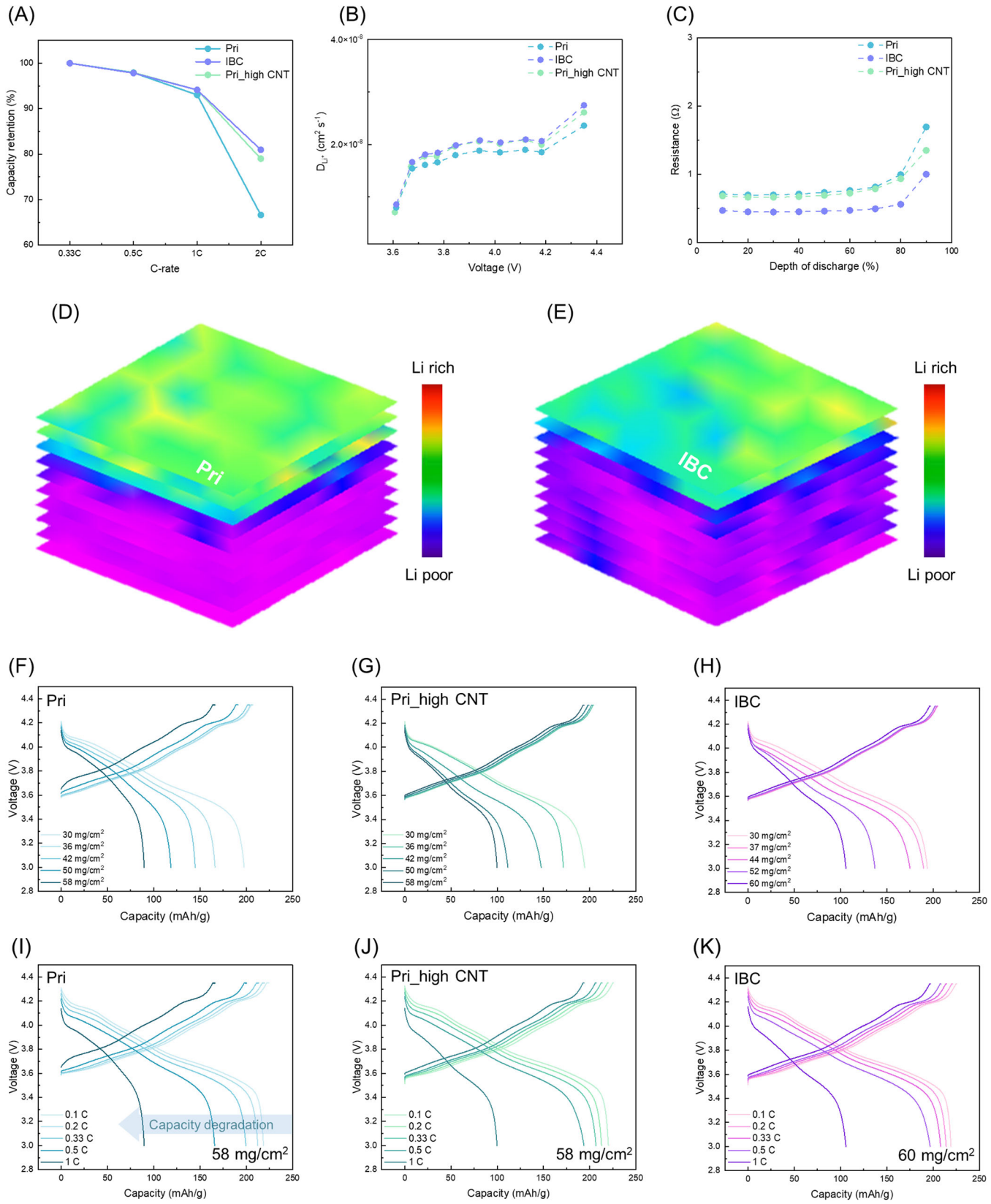


**FIGURE 4** | Correlation between rate capability and $Li^+$ diffusion behavior. (A) Rate capability with the half-cell. (B) GITT analysis at various voltages. (C) DC-IR results at depth of discharge. (D, E) 3D Li elemental mapping using LIBS at 3.2 g $cc^{-1}$ electrode after 2 C-rate discharge. (F–H) 1 C rate discharge capacity curve at various mass loadings. (I–K) High-mass-loading (60 mg $cm^{-2}$) charge-discharge curve at various C-rates.

the characterization of the rate performance for various loadings from 30 mg cm$^{-2}$ ( > 6 mAh cm$^{-2}$) to 60 mg cm$^{-2}$ ( > 12 mAh cm$^{-2}$) (Figure 4F–H), the IBC solution-applied electrode showed higher Coulombic efficiency than that of the pristine_high CNT-applied electrode. Generally, as the mass loading increases, the diffusion path of the $Li^+$ ion becomes longer and difficult to diffuse into the bottom of the electrode [44]. However, the IBC solution-applied electrode with a uniform CBD distribution improved the limitations of the high-mass-loading electrode by facilitating $Li^+$ ion diffusion based on the CNT domains at the bottom of the electrode. Furthermore, in the investigation of the capacity retention of the thick electrode (mass loading ~60 mg cm$^{-2}$) at various C-rates (Figure 4I–K), the IBC solution-applied electrode showed a higher discharge capacity at all C-rates than the pristine-applied electrode and pristine_high CNT-applied electrodes. Even at a 1 C rate, a difference in the discharge capacity of about 6% ~ 19% was observed; pristine-applied electrode: 89 mAh g$^{-1}$, pristine_high CNT-applied electrode: 100 mAh g$^{-1}$, and IBC solution-applied electrode: 106 mAh g$^{-1}$.

In the cycling performance, the initial Coulombic efficiencies of the IBC solution-applied electrode and the pristine_high CNT electrode were 80.65% and 80.24%, respectively, and there was no significant difference (Figure 5A). The rapid capacity degradation in the initial cycles (2–5 cycles) can be attributed to the lower initial irreversibility caused by the activation of Si particles in the anode (Figure S16) [45, 46]. In the long-term cycling test, the IBC solution-applied electrode (28 mg cm$^{-2}$, 5.6 mAh cm$^{-2}$) shows stable cycling performance with a capacity retention of 77.6% after 200 cycles, whereas pristine_high CNT shows 68.4% capacity retention. Long-term stability of IBC solution-applied electrodes was identically represented in both coin cells (up to 50 mg cm$^{-2}$, 10 mAh cm$^{-2}$) and pouch cells (30 mg cm$^{-2}$, 6 mh cm$^{-2}$) with higher mass loading (Figures S17 and S18). Additionally, the pouch cell manufactured for cycling tests achieved a specific energy of 326 Wh kg$^{-1}$ (Table S1). After cycling, the IBC solution-applied electrode showed excellent stability compared to the pristine-applied electrode (Figure 5B–F). The excellent cycle stability can be attributed to the uniform CBD distribution in the IBC solution-applied electrode and is supported by the ex situ X-ray diffraction (XRD) pattern results after 200 cycling. Both the pristine-applied electrode and the IBC solution-applied electrode showed typical peaks (003, 101, 104, 006/102, and 108/110) appearing in the layered structure of NCM811 before and after cycling [47, 48]. In general, the 003 peak shifts to the left or decreases in intensity due to delithiation, while it shifts to the right and increases in intensity owing to lithium insertion. The changes in the XRD patterns represented the repetitive volume change such as expansion and shrinkage in the electrode during charge/discharge of NCM-type LIBs. The leftward shift and intensity decrease of the 003 peak of the pristine-applied electrode after long-term cycling indicate that the NCM811's interplanar distance has decreased, its layered structure has compressed and this eventually may cause cracks in the electrode material due to stress caused by the repetitive volume change during cycling [49, 50]. On the other hand, the ex situ XRD patterns of the IBC solution-applied electrode showed a very small left shift and intensity decrease of the 003 peak and it was confirmed that the cracks of the electrode material would be minimized because the stress was evenly distributed throughout the electrode even with repeated volume changes during the charge/discharge process. Indeed, in the cross-sectional images of the IBC solution-applied electrode and the pristine-applied electrode after cycling, the particles showed dense packing before cycling and showed grain boundaries between them. As expected, many inter/intragranular cracks were formed and propagated in the cycled pristine-applied electrode [51]. In contrast, the micro-crack was suppressed in the IBC solution-applied electrode by suppressing particle degradation.

## 3 | Conclusion

In conclusion, we successfully fabricated a slurry with 77 wt% of total solid contents and a uniform CBD distribution based on an IBC solution and systemically investigated the IBC solution's effect on the performance of LIBs. In rheological characterization, it was found that the IBC solution-applied slurry is effective for dispersibility even in a high-concentration slurry, and IBC solution-applied electrodes eventually showed a uniform CBD distribution by inhibiting binder migration even after the drying process in the EPMA analysis. Furthermore, the prepared electrodes showed excellent adhesive properties and low electrical resistance. In many previous studies, the electrochemical performances of high-mass-loading electrodes have been investigated by evaluating electrodes containing excessive conductive additives and binders from 5 to 10 wt% of active materials. However, as electrodes containing such excessive sub-materials pose limitations in terms of practical electrode design, we fabricated electrodes with a few amounts of conductive additive and binder for reliability in practical battery applications. The manufactured IBC solution-applied electrode showed superior rate capability and cycle stability in the electrochemical performance evaluation. In addition, the IBC solution-applied thick electrodes ( > 12 mAh cm$^{-2}$) showed excellent rate capability compared to the pristine-applied thick electrode, even at relatively low conductive additive ratios; active material of 97.78 wt%, conductive additive of 0.6 wt%, binder of 1.5 wt%, and electrode loading density from 30 to 60 mg cm$^{-2}$. Therefore, it can be emphasized that the realization of a uniform CBD distribution within the electrode is directly related to the determination of the electrochemical performance in high-mass-loading LIBs and it is confirmed that the IBC solution-based approach is not only a practical approach for high-mass-loading LIBs with a uniform CBD distribution but also with high potential for introduction of various active materials, conductive additives, and binders in high-energy-density LIBs application. From an industrial perspective, the fabrication of a high-concentration slurry can ultimately enable the production of high-quality electrodes and a reduction in the loss rate, because of a series of reasons: reduction of the NMP solvent content in the mixing process, high-quality coating by reducing the side-edge effect in the coating process, and decrease in binder migration in the drying process. Beyond the industrial perspective, the realization of the reduction of NMP solvent contents via the fabrication of a high-concentration slurry is economically efficient and environmentally friendly, owing to the direct association with the reduction of installation costs, processing costs, processing time, and energy in the drying and recovery process.

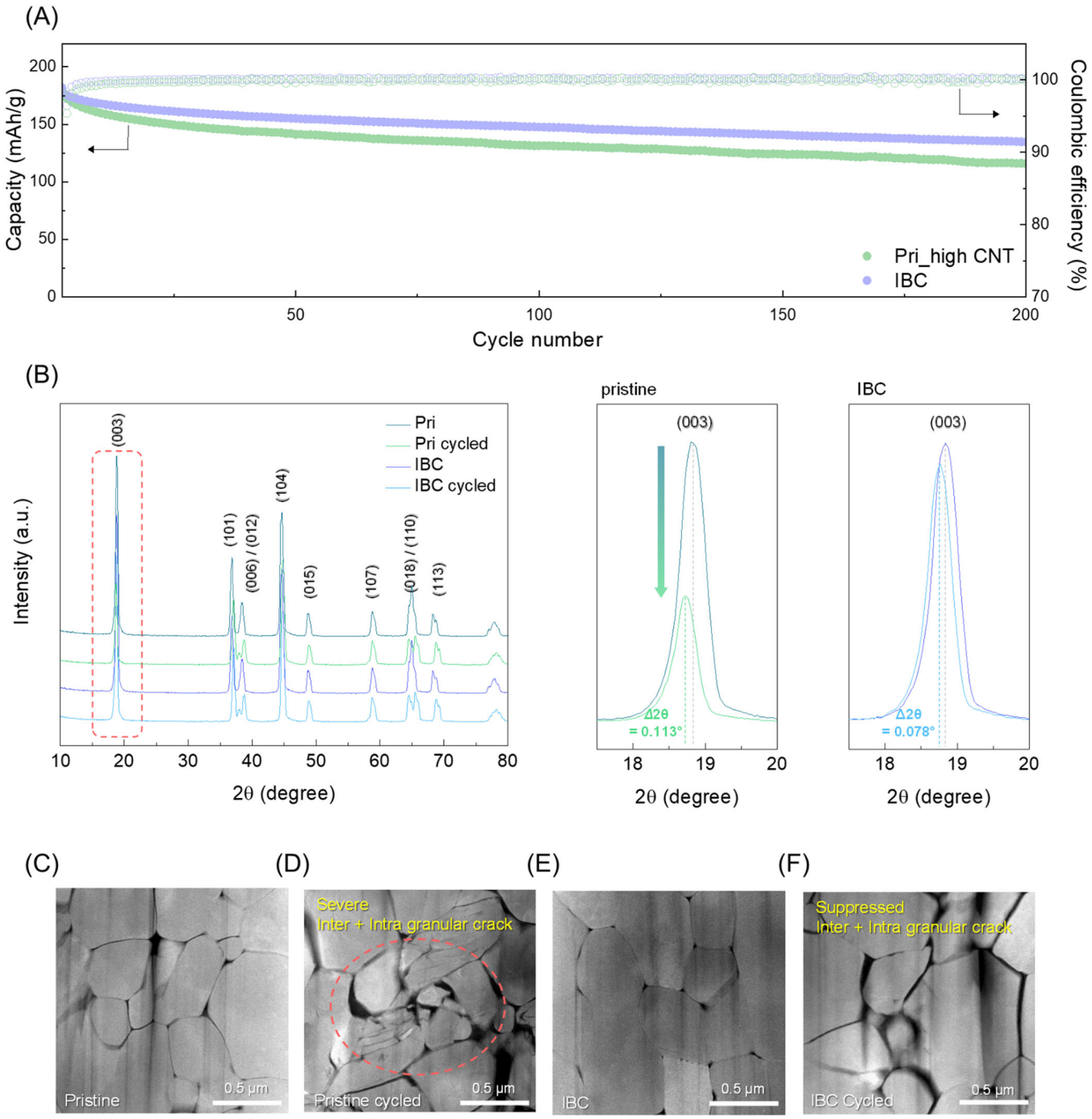


**FIGURE 5** | Cycling properties and post-cycling characteristics. (A) Comparison of the long-term cycling performance with graphite and Si/C anodes at a charge/discharge C-rate of 0.33/0.33 C at a voltage range of 2.8-4.2 V. (B) Ex situ XRD patterns analysis (C, F) Cross-sectional STEM images of before and after cycling: (C, D) pristine-applied electrode and (E, F) IBC solution-applied electrode. Cross-sectional images were obtained using the FIB technique, resulting in a curtain effect showing the milling artifact in the porous region.

## 4 | Experimental Section

### 4.1 | Materials

$LiNi_{0.8}Co_{0.1}Mn_{0.1}O_2$ (NCM811) was purchased from POSCO. MWCNTs (BT1003M) were purchased from LG Chem (Korea). A PVDF (Solef 5130) binder was obtained from Solvay Co., and IBC solution, which includes MWCNTs, PVDF, and a dispersant (hydrogenated nitrile butadiene rubber, HNBR), was dispersed in n-methyl-2-pyrrolidone (NMP) by Advanced Nano Products Co. Ltd. (Korea).

### 4.2 | Electrode Preparation

To compare the individual solution and IBC solution, all processes were performed under the same conditions. The slurries were prepared by mixing 200 g of NCM811 with MWCNTs and

PVDF in specified ratios using a homo-disper (HD2.5, PRIMIX) at 3000 rpm for 15 min in NMP. These slurries were coated onto Al foils and dried using a roll-to-roll comma coater at 120°C for 1 min (Figure S19). Dried electrodes were stored at 120°C for 10 h in a vacuum oven. The electrode composition is presented in Table S2. The anode slurry was prepared by mixing graphite, Si/C, CMC, SBR, C65, SWCNT, and DI water in specific ratios using a Thinky mixer (ARE-310) at 1300 rpm for 15 min. The anode slurry was coated onto Cu foils and dried at 100°C for 10 h in a vacuum oven. The electrode composition is presented in Table S3. Anode 1 showed a specific capacity of 460 mAh $g^{-1}$ and was fabricated with a mass loading of 14 mg$^{-2}$ (6.2 mAh $cm^{-2}$) and 15 mg $cm^{-2}$ (6.6 mAh $cm^{-2}$). Anode 2 showed a specific capacity of 621 mAh $g^{-1}$ and was fabricated with a mass loading of 14.7 mg $cm^{-2}$ (8.8 mAh $cm^{-2}$) and 18.4 mg $cm^{-2}$ (11 mAh $cm^{-2}$).

### 4.3 | Electrochemical Characterization

For the half-cell test, coin cells (CR2032), a PP separator (Celgard 2400), a Li metal (Wellcos Co.) counter electrode, and an electrolyte (1 M $LiPF_6$ in EC/DMC = 1:1 (v/v)) were assembled in a glovebox under high-purity Ar conditions. Rate capability and the galvanostatic intermittent titration technique (GITT) were performed in the voltage range of 3–4.35 V at 25°C. In addition, we compared $Li^+$ ion diffusion in half-cells by setting pristine_high CNT, which contains 40% more CNT than the pristine electrode and the IBC solution-applied electrode, as a control. Long-term cycling stability and Direct current internal resistance (DC-IR) were performed with graphite and Si/C-based anodes with a 1.1 N/P ratio as counter electrodes. For the DC-IR test, pouch cells ($40 \times 50$ mm$^2$) were assembled in a dry room, and long-term cycling stability tests were also performed using the same specification pouch cells and CR2032 coin cell. All cells were tested using the WBCS 3000 battery tester system (WonA Tech), following the constant current-constant voltage (CC-CV) procedure. Two pre-cycles at 0.1 C were performed as a formation step for all cells before the test. This was conducted at a fixed charge rate of 0.33 C at various discharge rates from 0.33 to 2 C.

### 4.4 | Structural and Physicochemical Characterization

The rheological properties were measured using the TA instrument discovery HR-3. The shear viscosity was measured at room temperature at shear rates varying from 0.01 to 1000 $s^{-1}$. The phase angle was measured at an angular frequency of 6.3 rad $s^{-1}$ and a strain of 0.1%.

The slurry coating profile system consists of three main components: a linear stage for moving the substrate, a laser displacement sensor with a moving mount stage, and a coating blade with a stand. The cathode slurry is deposited on an aluminum foil (1085-H18; Wellcos Co.) mounted on a high-precision linear motor (V-508; Physik Instrumente GmbH & Co. Kg, Karlsruhe, Germany) with a metal plate. The linear stage enables the induced coating flow to occur under conditions similar to those used in the commercial battery electrode manufacturing process by accurately controlling the substrate speed up to 600 mm $s^{-1}$. The laser displacement sensor can measure the cathode slurry thickness deposited on the aluminum foil by measuring the displacement of the coating layer surface through the laser triangulation method. As the laser displacement sensor can only measure the displacement to a certain point, we measured the cross-web thickness profile of the cathode slurry wet film using a moving mount stage that allows the displacement sensor to perform cross-web directional movement ($y$-direction). The coating blade used in this study was designed to have a similar geometry to the downstream lip region of the slot die. The coating blade was made of stainless steel (SUS630) and was custom-made by Changsung Tech. In this experiment, electrodes were fabricated using a coating blade with a blade lip of 260 and 350 μm at a coating speed of 3 m $min^{-1}$.

Drying rate measurements were performed using a moisture analyzer (MB90, OHAUS). Electrodes coated with 70 wt% and 77 wt% slurries were analyzed for weight change over time using a moisture analyzer. The analysis conditions included ramping the temperature to 120°C at a rate of 2°C $s^{-1}$ and holding the temperature for 1 min.

90° peel tests were conducted using a universal testing machine (LS-1; LLOYD Instruments) at a fixed rate of 300 mm $min^{-1}$. In the adhesion test, the electrode attached to the double-sided tape measured 20 mm, and the Al foil was separated from the electrode during the test. The average forces were calculated within the middle region (20%–80% of the separated range). In the cohesion test, one-sided scotch tape was attached to the left electrode on the double-sided tape (direction of aluminum foil removal), and the forces were measured as the tape separated with a small amount of electrode on the double-sided tape; the procedure was repeated several times.

The resistances of the electrodes were measured using a Hioki electrode resistance meter (XF-057). A constant current (10 mA) was applied to the calendared electrode, and the potential change between the multiprobe was measured and calculated. The Al foil's resistivity and thickness for calculations were $2.65 \times 10^{-6}$ Ω cm and 20 μm, respectively.

XRD was performed using PANalytical Empyrean with Mo Kα radiation ($\lambda = 0.70931$ Å). The $2\theta$ range was 5°–35° with a step size of 0.016°. Then, the $2\theta$ angles of XRD patterns were converted with Cu Kα radiation ($\lambda = 1.54178$ Å) for comparison with other studies [52, 53].

Scanning electron microscopy (SEM) images were observed using a JSM-6700F (JEOL) under an accelerating voltage of 10 kV. The electrodes were treated by a cross-section polisher using IB-19520CCP (JEOL) to obtain the cross-section polisher-scanning electron microscope images. The electron probe micro-analysis images were observed and analyzed using JXA-8500F (JEOL) under an accelerating voltage of 15 kV.

Cross-sectional scanning transmission electron microscope (STEM) images were obtained using field-emission transmission electron microscopy (FE-TEM: JEM-ARM200F; JEOL Ltd.) under an accelerating voltage of 200 kV. The particles were cross-milled by a focused ion beam (FIB) using crossbeam-540 (ZEISS).

To obtain the distribution of Li, the electrodes were prepared after a 2 C-rate discharge. The discharged cell was disassembled, and the cathode (14-pi) was rinsed with a solvent (DMC) to remove residual salts in an argon-filled glovebox. Laser-induced breakdown (LIBS) images were observed using a Tandem Laser Ablation LIBS (J200; Aplied Spectra, Inc.). The J200 LIBS system consists of a Nd/YAG-ns 1064 nm laser and operates at 15 mJ, spot size 100 μm, under argon. The laser was continuously irradiated until the active material layer was ablated and the Al foil was observed. 49 spots were measured across the electrode surface, and data were extracted from 25 spots located in a 1 mm × 1 mm area in the center of the sample. Using LIBS data from the same area, we determined the depth-dependent lithium distribution. Also, 3D mapping was generated with a detailed visualization of lithium distribution and concentration gradients within the electrode.


## Acknowledgments

J.K.P., W.S., and W.J. contributed equally to this study. The authors thank Trinity Engineering for supporting electrode 3D modeling based on the 3D reconstruction function in the Geodict software. This study was supported by the National Research Foundation of Korea (NRF) grant funded by the Korea government (MSIT) (No. 2022M3H4A6A0103720142), the National Research Council of Science & Technology (NST) grant by the Korea government (MSIT) (No. GTL24011-000), and the Technology Innovation Program (RS-2024-00404165) through the Korea Planning & Evaluation Institute of Industrial Technology (KEIT) funded by the Ministry of Trade, Industry & Energy (MOTIE, Korea). This study was also supported by the Samsung SDI Co. Ltd. and the Korea Institute of Science and Technology (KIST) institutional program (2E33942, 2E3394B).


## Conflicts of Interest

The authors declare no conflicts of interest.

## References


1. A. Kraytsberg and Y. Ein-Eli, "Higher, Stronger, Better... A Review of 5 Volt Cathode Materials for Advanced Lithium-Ion Batteries," *Advanced Energy Materials* 2, no. 8 (2012): 922–939.

2. M. Hu, X. Pang, and Z. Zhou, "Recent Progress in High-Voltage Lithium Ion Batteries," *Journal of Power Sources* 237 (2013): 229–242.

3. J. Xiang, Y. Wei, Y. Zhong, et al., "Building Practical High-Voltage Cathode Materials for Lithium-Ion Batteries," *Advanced Materials* 34, no. 52 (2022): 2200912.

4. H. Niu, N. Zhang, Y. Lu, et al., "Strategies Toward the Development of High-Energy-Density Lithium Batteries," *Journal of Energy Storage* 88 (2024): 111666.

5. J. Ahn, B. Park, J. Kim, M. K. Um, J. W. Yi, and J. K. Yoo, ""Multifunctional Additives for High-Energy-Density Lithium-Ion Batteries: Improved Conductive Additive/Binder Networks and Enhanced Electrochemical Properties," *ACS Applied Materials & Interfaces* 13, no. 17 (2021): 19970–19982.

6. J.-K. Yoo, Y. Oh, T. Park, K. E. Lee, M. K. Um, and J. W. Yi, "Optimization of Carbon Nanotubes as Conductive Additives for High-Energy-Density Electrodes for Lithium-Ion Batteries," *Energy Technology* 7, no. 5 (2019): 1800845.

7. L. Deng, J. K. Liu, Z. Wang, et al., "A Formula to Customize Cathode Binder for Lithium Ion Battery," *Advanced Energy Materials* 14, no. 40 (2024): 2401514.

8. S. Tanaka, T. Narutomi, S. Suzuki, A. Nakao, H. Oji, and N. Yabuuchi, "Acrylonitrile-Grafted Poly (Vinyl Alcohol) Copolymer as Effective Binder for High-Voltage Spinel Positive Electrode," *Journal of Power Sources* 358 (2017): 121–127.

9. A. C. Rolandi, I. de Meatza, N. Casado, M. Forsyth, D. Mecerreyes, and C. Pozo-Gonzalo, "Unlocking Sustainable Power: Advances in Aqueous Processing and Water-Soluble Binders for NMC Cathodes in High-Voltage Li-Ion Batteries," *RSC Sustainability* 2, no. 8 (2024): 2125–2149.

10. H. Li, L. Peng, D. Wu, J. Wu, Y. Zhu, and X. Hu, "Ultrahigh-Capacity and Fire-Resistant $LiFePO_4$-Based Composite Cathodes for Advanced Lithium-Ion Batteries," *Advanced Energy Materials* 9, no. 10 (2019): 1802930.

11. Y. Xia, T. S. Mathis, M.-Q. Zhao, et al., "Thickness-Independent Capacitance of Vertically Aligned Liquid-Crystalline Mxenes," *Nature* 557, no. 7705 (2018): 409–412.

12. H. J. Peng, J. Q. Huang, X. B. Cheng, and Q. Zhang, "Review on High-Loading and High-Energy Lithium–Sulfur Batteries," *Advanced Energy Materials* 7, no. 24 (2017): 1700260.

13. H. Sun, J. Zhu, D. Baumann, et al., "Hierarchical 3D Electrodes for Electrochemical Energy Storage," *Nature Reviews Materials* 4, no. 1 (2019): 45–60.

14. M. Jiang, D. L. Danilov, R. A. Eichel, and P. H. L. Notten, "A Review of Degradation Mechanisms and Recent Achievements for Ni-Rich Cathode-Based Li-Ion Batteries," *Advanced Energy Materials* 11, no. 48 (2021): 2103005.

15. Q. Zhao, Z. Zhang, D. Song, et al., "Stabilizing the Interphase in an Ultra-High-Nickel Cathode Enabling High-Performance Lithium-Ion Batteries," *ACS Applied Materials & Interfaces* 16, no. 37 (2024): 49227–49235.

16. Y. Kuang, C. Chen, D. Kirsch, and L. Hu, "Thick Electrode Batteries: Principles, Opportunities, and Challenges," *Advanced Energy Materials* 9, no. 33 (2019): 1901457.

17. K. Fu, X. Li, K. Sun, et al., "Rational Design of Thick Electrodes in Lithium-Ion Batteries by Re-Understanding the Relationship Between Thermodynamics and Kinetics," *Advanced Functional Materials* 34, no. 51 (2024): 2409623.

18. K. G. Gallagher and P. A. Nelson, *Lithium-Ion Batteries* (Elsevier, 2014), 97–126.

19. J. Li, Z. Du, R. E. Ruther, et al., "Toward Low-Cost, High-Energy Density, and High-Power Density Lithium-Ion Batteries," *JOM* 69 (2017): 1484–1496.

20. W. B. Hawley and J. Li, "Electrode Manufacturing for Lithium-Ion Batteries—Analysis of Current and Next Generation Processing," *Journal of Energy Storage* 25 (2019): 100862.

21. J. Entwistle, R. Ge, K. Pardikar, R. Smith, and D. Cumming, "Carbon Binder Domain Networks and Electrical Conductivity in Lithium-Ion Battery Electrodes: A Critical Review," *Renewable and Sustainable Energy Reviews* 166 (2022): 112624.

22. J. H. Chang, M. W. Pin, I. Kim, et al., "Binder Migration: Frequently Observed yet Overlooked Phenomena in Electrode Processing for Lithium-Ion Batteries," *Journal of Energy Storage* 83 (2024): 110729.

23. J. Ahn, H.-G. Im, Y. Lee, et al., "A Novel Organosilicon-Type Binder for $LiCoO_2$ Cathode in Li-Ion Batteries," *Energy Storage Materials* 49 (2022): 58–66.

24. S. Spiegel, T. Heckmann, A. Altvater, R. Diehm, P. Scharfer, and W. Schabel, "Investigation of Edge Formation During the Coating Process of Li-Ion Battery Electrodes," *Journal of Coatings Technology and Research* 19 (2022): 121–130.

25. W. B. Hawley and J. Li, "Beneficial Rheological Properties of Lithium-Ion Battery Cathode Slurries From Elevated Mixing and Coating Temperatures," *Journal of Energy Storage* 26 (2019): 100994.

26. R. Gordon, M. Kassar, and N. Willenbacher, "Effect of Polymeric Binders on Dispersion of Active Particles in Aqueous $LiFePo_4$-Based

Cathode Slurries as Well as on Mechanical and Electrical Properties of Corresponding Dry Layers," *ACS Omega* 5, no. 20 (2020): 11455–11465.

27. B. Zhao, D. Yin, Y. Gao, and J. Ren, "Concentration Dependence of Yield Stress, Thixotropy, and Viscoelasticity Rheological Behavior of Lithium-Ion Battery Slurry," *Ceramics International* 48, no. 13 (2022): 19073–19080.

28. L. Sun, X. Zhang, W. Tan, M. Zhu, R. Liu, and C. Li, "Rheology of Pyrite Slurry and Its Dispersant for the Biooxidation Process," *Hydrometallurgy* 104, no. 2 (2010): 178–185.

29. N. Casson, "Flow Equation for Pigment-Oil Suspensions of the Printing Ink-Type," in *Rheology of Disperse Systems* (Pergamon Press, 1959), 84–104.

30. K. Bhamidipati, S. Didari, and T. A. L. Harris, "Experimental Study on Air Entrainment in Slot Die Coating of High-Viscosity, Shear-Thinning Fluids," *Chemical Engineering Science* 80 (2012): 195–204.

31. M. Lee, W. Jo, D. Kim, et al., "Analysis of Side Heavy Edge Reduction of Battery Electrode Using High Speed Blade Coating Process," *Journal of Power Sources* 598 (2024): 234135.

32. C. D. Reynolds, S. D. Hare, P. R. Slater, M. J. H. Simmons, and E. Kendrick, "Rheology and Structure of Lithium-Ion Battery Electrode Slurries," *Energy Technology* 10, no. 10 (2022): 2200545.

33. L. Ouyang, Z. Wu, J. Wang, et al., "The Effect of Solid Content on the Rheological Properties and Microstructures of a Li-Ion Battery Cathode Slurry," *RSC Advances* 10, no. 33 (2020): 19360–19370.

34. D. Burger, J. Klemens, N. Keim, et al., "Additive Influence on Binder Migration in Electrode Drying," *Energy Technology* 12, no. 7 (2024): 2400057.

35. C. D. Reynolds, H. Walker, A. Mahgoub, E. Adebayo, and E. Kendrick, "Battery Electrode Slurry Rheology and Its Impact on Manufacturing," *Energy Advances* 4, no. 1 (2025): 84–93.

36. M. Schmitt, P. Scharfer, and W. Schabel, "Slot Die Coating of Lithium-Ion Battery Electrodes: Investigations on Edge Effect Issues for Stripe and Pattern Coatings," *Journal of Coatings Technology and Research* 11 (2014): 57–63.

37. A. Kraytsberg and Y. Ein-Eli, "Conveying Advanced Li-Ion Battery Materials Into Practice the Impact of Electrode Slurry Preparation Skills," *Advanced Energy Materials* 6, no. 21 (2016): 1600655.

38. D. L. Wood, J. D. Quass, J. Li, S. Ahmed, D. Ventola, and C. Daniel, "Technical and Economic Analysis of Solvent-Based Lithium-Ion Electrode Drying With Water and NMP," *Drying Technology* 36, no. 2 (2018): 234–244.

39. G.-W. Lee, J. H. Ryu, W. Han, K. H. Ahn, and S. M. Oh, "Effect of Slurry Preparation Process on Electrochemical Performances of $LiCoO_2$ Composite Electrode," *Journal of Power Sources* 195, no. 18 (2010): 6049–6054.

40. J. Kim, S. Park, S. Hwang, and W.-S. Yoon, "Principles and Applications of Galvanostatic Intermittent Titration Technique for Lithium-Ion Batteries," *Journal of Electrochemical Science and Technology* 13, no. 1 (2022): 19–31.

41. A. Eftekhari, "Lithium-Ion Batteries With High Rate Capabilities," *ACS Sustainable Chemistry & Engineering* 5, no. 4 (2017): 2799–2816.

42. J. Lei, F. McLarnon, and R. Kostecki, "In Situ Raman Microscopy of Individual $LiNi_{0.8}Co_{0.15}Al_{0.05}O_2$ Particles in a Li-Ion Battery Composite Cathode," *Journal of Physical Chemistry B* 109, no. 2 (2005): 952–957.

43. H. Cha, J. Kim, H. Lee, et al., "Boosting Reaction Homogeneity in High-Energy Lithium-Ion Battery Cathode Materials," *Advanced Materials* 32, no. 39 (2020): 2003040.

44. H. Gao, Q. Wu, Y. Hu, J. P. Zheng, K. Amine, and Z. Chen, "Revealing the Rate-Limiting Li-Ion Diffusion Pathway in Ultrathick Electrodes for Li-Ion Batteries," *Journal of Physical Chemistry Letters* 9, no. 17 (2018): 5100–5104.

45. Y. Jin, B. Zhu, Z. Lu, N. Liu, and J. Zhu, "Challenges and Recent Progress in the Development of Si Anodes for Lithium-Ion Battery," *Advanced Energy Materials* 7, no. 23 (2017): 1700715.

46. A. L. Michan, G. Divitini, A. J. Pell, M. Leskes, C. Ducati, and C. P. Grey, "Solid Electrolyte Interphase Growth and Capacity Loss in Silicon Electrodes," *Journal of the American Chemical Society* 138, no. 25 (2016): 7918–7931.

47. M. A. M. M. Al-samet and E. Burgaz, "A Novel Coating Layer of Mesoporous Silica on $LiNi_{0.8}Co_{0.1}Mn_{0.1}O_2$ (NCM811) Cathode Material for Advanced Lithium-Ion Batteries," *Electrochimica Acta* 507 (2024): 145167.

48. H. Yang, K. Wu, G. Hu, Z. Peng, Y. Cao, and K. Du, "Design and Synthesis of Double-Functional Polymer Composite Layer Coating to Enhance the Electrochemical Performance of the Ni-Rich Cathode at the Upper Cutoff Voltage," *ACS Applied Materials & Interfaces* 11, no. 8 (2019): 8556–8566.

49. Y. Wu, Z. Zeng, M. Liu, et al., "Restraining Lattice Oxygen Escape by Bioinspired Antioxidant Enables Thermal Runaway Prevention in Ni-Rich Cathode Based Lithium-Ion Batteries," *Advanced Energy Materials* 14, no. 31 (2024): 2401037.

50. N. Y. Kim, J. Moon, M. H. Ryou, et al., "Amphiphilic Bottlebrush Polymeric Binders for High-Mass-Loading Cathodes in Lithium-Ion Batteries," *Advanced Energy Materials* 12, no. 1 (2022): 2102109.

51. T. M. M. Heenan, A. Wade, C. Tan, et al., "Identifying the Origins of Microstructural Defects Such as Cracking Within Ni-Rich NMC811 Cathode Particles for Lithium-Ion Batteries," *Advanced Energy Materials* 10, no. 47 (2020): 2002655.

52. N.-Y. Park, G.-T. Park, S.-B. Kim, W. Jung, B. C. Park, and Y. K. Sun, "Degradation Mechanism of Ni-Rich Cathode Materials: Focusing on Particle Interior," *ACS Energy Letters* 7, no. 7 (2022): 2362–2369.

53. S. S. Zhang, "Understanding of Performance Degradation of $LiNi_{0.80}Co_{0.10}Mn_{0.10}O_2$ Cathode Material Operating at High Potentials," *Journal of Energy Chemistry* 41 (2020): 135–141.

## Supporting Information

Additional supporting information can be found online in the Supporting Information section.
Carbon Energy Supporting Information_Formatting revision CEY2-2025-0164.